An Analytical and Numerical Study of Acoustic Mismatch Effects on Internal Dielectrically Transduced MEMS Resonators

Eugene Hwang, *Student Member, IEEE*, and Sunil A. Bhave, *Member, IEEE*

***Abstract*—This paper presents a supplement to the 1-D theory of internal dielectric transduction by including the effects of acoustic mismatch on the resonant frequency and motional impedance of internal dielectrically transduced micromechanical resonators. Analytical expressions for the mode shapes in said resonators are mathematically derived and verified for various dielectric and resonator body materials by comparing numerical simulation results with finite element analysis results using commercial software. Correction factors to the resonant frequencies and motional impedances predicted by the original theory are presented to provide designers a simple yet accurate model that takes into account the effects of acoustic mismatch. Our analysis shows that the ratio of Young's moduli of the dielectric film and resonator body materials significantly impacts the motional impedance and thus must be considered when choosing the optimal dielectric material. This modified model will allow for precise and optimal design of internal dielectrically transduced micromechanical resonators for applications up to tens of gigahertz.**

I. Introduction

Recent progress in the area of RF microelectromechanical systems (MEMS) resonators has pushed operating frequencies into the gigahertz range while steadily lowering the motional impedance through various design techniques, including large-scale resonator arrays and the use of piezoelectric transduction [1], [2]. Such resonators present the possibility for high-Q, integrated filters and low phase noise, monolithic frequency references. Recently, it has been shown [3] that optimal transduction of an internal dielectrically transduced resonator scales favorably with increasing frequency up to tens of gigahertz, demonstrating the potential for low-impedance silicon micromechanical resonators at millimeter-wave frequencies. In fact, such transduction methods are used in [4] to demonstrate both the highest $f \cdot Q$ product and the highest resonant frequency reported in an electrostatically transduced polysilicon resonator to date.

One obstacle to the wide-spread adoption of such devices is the absence of reliable modeling. For simplicity, most micromechanical devices are modeled by simple 1-D theoretical models. This results in discrepancy between the experimental and predicted behavior of these resonators. The reasons for this discrepancy can be largely divided into systematic (e.g., lateral inertia effects) and random sources (e.g., process variations). In this paper, we focus on analytical modeling of internal dielectrically transduced resonators. In particular, the use of a solid transduction dielectric film introduces a predictable source of discrepancy that arises from the acoustic mismatch between the resonator body and the dielectric film. This paper quantifies the effects of acoustic mismatch on resonator properties and allows for the precise and optimal design of internal dielectrically transduced micromechanical resonators.

In Section II, we set up the equations of motion for a free-free composite resonator with three distinct regions and derive analytical expressions for the mode shape. In Section III, we present numerical simulation results of our theory. In this section, we also discuss, based on the results of these simulations, the impact of acoustic mismatch on the characteristics of the internal dielectrically transduced resonator. Finally, we present correction factors that can be used by the designer to accurately predict the behavior of such resonators.

II. Composite Bar Resonator Theory

Here, we develop the theory for an electrostatically transduced composite bar resonator. Fig. 1 shows the structure that will be used in the development of this theory. The structure is actuated by the capacitive force across the dielectric transducer. This yields a force distribution represented by two delta functions at the interfaces between the dielectric and resonator structure. These forcing functions are equal in magnitude but opposite in direction. Because of the complexity of the full analysis, we make a few simplifying assumptions to aid in the development of this theory. First, we assume zero displacement at the center, i.e., the center is tethered. Also, we assume a symmetric structure and mode shape about the center, allowing consideration of only half the resonator. And finally, we assume only 1-D longitudinal motion. Note that this theory is only applicable to bar resonators but gives insight into the general effects of acoustic mismatch in similar composite bulk-mode devices like those in [5] and [6].

The analysis begins by first dividing half of the resonator into three sections: the inner body, the dielectric film, and the electrode. These sections will be denoted in subsequent equations by subscripts 1, 2, and 3, respectively.

Manuscript received June 18, 2009; accepted April 5, 2010.

The authors are with Cornell University, School of Electrical and Computer Engineering, Ithaca, NY (e-mail: eoh3@cornell.edu).

Digital Object Identifier 10.1109/TUFFC.2010.1597

Fig. 1 indicates the initial coordinate systems used in each region to simplify the analysis. This analysis utilizes linearity to find the overall response of the system as the sum of impulse responses arising from excitations at each dielectric interface. The three coupled forced wave equations are

$$\left[\rho_{\rm si}\frac{\partial^2}{\partial t^2} - b_{\rm si}\frac{\partial^3}{\partial t \partial {x_1}^2} - E_{\rm si}\frac{\partial^2}{\partial {x_1}^2}\right]u_1(x_1,t) = q_1(x_1,t) \quad (1)$$

$$\left[\rho_{\rm diel}\frac{\partial^2}{\partial t^2} - b_{\rm diel}\frac{\partial^3}{\partial t \partial {x_2}^2} - E_{\rm diel}\frac{\partial^2}{\partial {x_2}^2}\right]u_2(x_2,t) = q_2(x_2,t) \quad (2)$$

$$\left[\rho_{\rm si}\frac{\partial^2}{\partial t^2} - b_{\rm si}\frac{\partial^3}{\partial t \partial {x_3}^2} - E_{\rm si}\frac{\partial^2}{\partial {x_3}^2}\right]u_3(x_3,t) = q_3(x_3,t). \quad (3)$$

In these equations, u_n are the solutions to the coupled forced wave equations within each region for input forcing functions q_n. It should be noted that these input forcing functions q_n are not equivalent to the actual external force applied to the resonator, but rather the force distribution, or $\partial f_n/\partial x$, where f_n is the external force throughout the structure. Kaajakari *et al.* also highlight this distinction in their model [7] and it is shown clearly in Fig. 1. E, b, and ρ represent the Young's modulus, damping factor, and density, respectively, within each region. If we assume time harmonic excitation, then q_n and u_n can be expressed as

$$q_n(x_n,t) = Q_n(x_n)e^{-j\omega t} \quad (4)$$

$$u_n(x_n,t) = U_n(x_n)e^{-j\omega t}\ . \quad (5)$$

This allows us to separate time-dependence from (1)–(3). Furthermore, if we define

$$Q_n(x_n) = \delta(x_n - \zeta_n), \quad (6)$$

then $U_n\,(x_n) \rightarrow G_n\,(x_n|\zeta_n)$, where G_n is the Green's function of the following coupled system of equations.

$$-\omega^2\rho_{\rm si} - \left(E_{\rm si} - j\omega b_{\rm si}\right)\frac{\partial^2 G_1(x_1|\zeta_1)}{\partial {x_1}^2} = \delta(x_1 - \zeta_1) \quad (7)$$

$$-\omega^2\rho_{\rm diel} - \left(E_{\rm diel} - j\omega b_{\rm diel}\right)\frac{\partial^2 G_2(x_2|\zeta_2)}{\partial {x_2}^2} = \delta(x_2 - \zeta_2) \quad (8)$$

$$-\omega^2\rho_{\rm si} - \left(E_{\rm si} - j\omega b_{\rm si}\right)\frac{\partial^2 G_3(x_3|\zeta_3)}{\partial {x_3}^2} = \delta(x_3 - \zeta_3). \quad (9)$$

To find the resonant frequencies, we will first consider the case where the system is lossless, or $b_{\rm si} = b_{\rm diel} = 0$. This can be done because we are assuming that the loss in the system is relatively low and thus its impact on the resonant frequency is small. In this case, the general Green's function solution in each region is a sum of sine and cosine terms, where $k_{\rm diel}$ and $k_{\rm si}$ are the wavenumbers in region 2 (dielectric) and regions 1 and 3 (resonator body and electrode), respectively. We assume here that all regions have a linear dispersion relationship as given by (13).

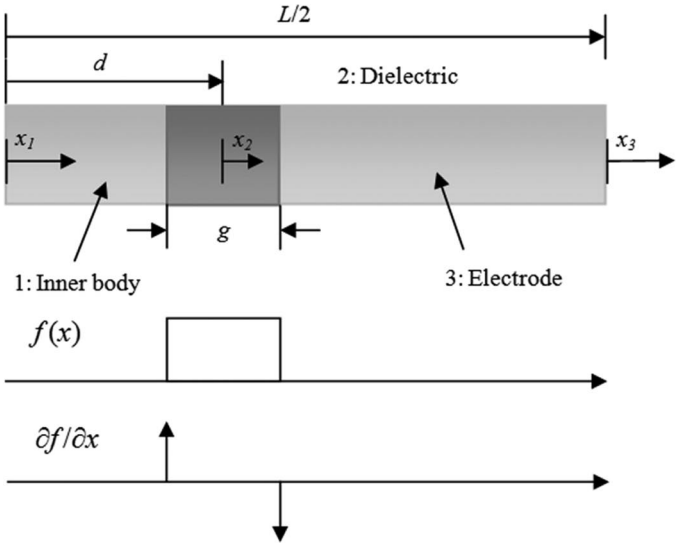

Fig. 1. Cross-section of composite resonator geometry and coordinate system. The external force input to the system and the resulting input forcing functions are shown in the axes below the resonator cross-section.

$$G_{1,i}(x_1|\zeta_1) = A_{1,i}(\zeta_1)\sin(k_{\rm si}x_1) + B_{1,i}(\zeta_1)\cos(k_{\rm si}x_1) \quad (10)$$

$$G_{2,i}(x_2|\zeta_2) = A_{2,i}(\zeta_2)\sin(k_{\rm diel}x_2) + B_{2,i}(\zeta_2)\cos(k_{\rm diel}x_2) \quad (11)$$

$$G_{3,i}(x_3|\zeta_3) = A_{3,i}(\zeta_3)\sin(k_{\rm si}x_3) + B_{3,i}(\zeta_3)\cos(k_{\rm si}x_3) \quad (12)$$

$$k_{\rm si} = \frac{\omega}{c_{\rm si}}, \quad k_{\rm diel} = \frac{\omega}{c_{\rm diel}} \quad (13)$$

Here $c_{\rm si}$ refers to the longitudinal acoustic velocities in regions 1 and 3 (resonator body and electrode) and $c_{\rm diel}$ refers to the longitudinal acoustic velocity in region 2 (dielectric). Because the force distribution we are concerned with consists of two delta functions, we employ the subscript i to specify the excitation location (either left for the force at the left dielectric interface or right for the force at the right dielectric interface) that produces the corresponding Green's function. Obtaining the coefficients in (10)–(12) can be done by applying boundary and continuity conditions. The boundary and continuity conditions arising from the impulse on the left dielectric interface for a free resonator are given by

$$G_{1,\rm left}(0) = 0 \quad (14)$$

$$\frac{dG_{3,\rm left}}{dx_3}(0) = 0 \quad (15)$$

$$G_{1,\rm left}(L_{\rm body}) = G_{2,\rm left}\left(-\frac{g}{2}\right) \quad (16)$$

$$G_{3,\rm left}(-L_{\rm elec}) = G_{2,\rm left}\left(\frac{g}{2}\right) \quad (17)$$

$$E_{\rm diel}\left.\frac{dG_{2,\rm left}}{dx_2}\right|_{x_2=-g/2} - E_{\rm si}\left.\frac{dG_{1,\rm left}}{dx_1}\right|_{x_1=L_{\rm body}} = -\frac{\varepsilon_0\varepsilon_r V_{\rm DC}}{g^2} \quad (18)$$

$$E_{\mathrm{si}}\left.\frac{dG_{3,\mathrm{left}}}{dx_3}\right|_{x_3=-L_{\mathrm{elec}}} - E_{\mathrm{diel}}\left.\frac{dG_{2,\mathrm{left}}}{dx_2}\right|_{x_2=g/2} = 0. \quad (19)$$

Here, L_{body} and L_{elec} are used for brevity and refer to the length of the inner body and the electrode, respectively. Specifically, $L_{\mathrm{body}} = d - g/2$ and $L_{\mathrm{elec}} = L/2 - d - g/2$. For an impulse on the right dielectric interface, (14)–(17) are still valid (with subscript left changed to right), but (18) and (19) change to (20) and (21).

$$E_{\mathrm{diel}}\left.\frac{dG_{2,\mathrm{right}}}{dx_2}\right|_{x_2=-g/2} - E_{\mathrm{si}}\left.\frac{dG_{1,\mathrm{right}}}{dx_1}\right|_{x_1=L_{\mathrm{body}}} = 0 \quad (20)$$

$$E_{\mathrm{si}}\left.\frac{dG_{3,\mathrm{right}}}{dx_3}\right|_{x_3=-L_{\mathrm{elec}}} - E_{\mathrm{diel}}\left.\frac{dG_{2,\mathrm{right}}}{dx_2}\right|_{x_2=g/2} = \frac{\varepsilon_0\varepsilon_r V_{\mathrm{DC}}}{g^2} \quad (21)$$

The results for each excitation are then summed to give the displacement $U_n(x_n)$ in each region

$$U_1(x_1) = G_{1,\mathrm{left}} + G_{1,\mathrm{right}} = A_1\sin(k_{\mathrm{si}}x_1) + B_1\cos(k_{\mathrm{si}}x_1) \quad (22)$$

$$U_2(x_2) = G_{2,\mathrm{left}} + G_{2,\mathrm{right}} = A_2\sin(k_{\mathrm{diel}}x_2) + B_2\cos(k_{\mathrm{diel}}x_2) \quad (23)$$

$$U_3(x_3) = G_{3,\mathrm{left}} + G_{3,\mathrm{right}} = A_3\sin(k_{\mathrm{si}}x_3) + B_3\cos(k_{\mathrm{si}}x_3). \quad (24)$$

The expressions for the mode shape in each region are given in (25)–(32). Note that D appears in common in all expressions. For the lossless case, there will be values of ω such that $D(\omega) = 0$, at which the amplitude coefficients approach infinity. These values of ω correspond to the resonant frequencies of the system. The finite values of these coefficients at the resonant frequencies are found when loss is included in the system, which will be considered numerically in the next section.

$$A_1 = \frac{2\varepsilon_0\varepsilon_r V_{\mathrm{DC}}\sin\left(k_{\mathrm{diel}}\frac{g}{2}\right)}{g^2}\frac{1}{E_{\mathrm{si}}k_{\mathrm{si}}}\frac{N_1}{D}, \quad B_1 = 0, \quad \text{where} \quad (25)$$

$$N_1 = \sqrt{\frac{E_{\mathrm{diel}}\rho_{\mathrm{diel}}}{E_{\mathrm{si}}\rho_{\mathrm{si}}}}\sin\left(k_{\mathrm{diel}}\frac{g}{2}\right)\cos\left(k_{\mathrm{si}}\left(\frac{g}{2} - \frac{L}{2} + d\right)\right) - \cos\left(k_{\mathrm{diel}}\frac{g}{2}\right)\sin\left(k_{\mathrm{si}}\left(\frac{g}{2} - \frac{L}{2} + d\right)\right) \quad (26)$$

$$A_2 = \frac{\varepsilon_0\varepsilon_r V_{\mathrm{DC}}}{g^2}\frac{1}{E_{\mathrm{si}}k_{\mathrm{si}}}\frac{N_{A2}}{D}, \quad B_2 = \frac{\varepsilon_0\varepsilon_r V_{\mathrm{DC}}}{g^2}\frac{1}{E_{\mathrm{si}}k_{\mathrm{si}}}\frac{N_{B2}}{D}, \quad \text{where} \quad (27)$$

$$N_{A2} = \cos\left(k_{\mathrm{diel}}\frac{g}{2}\right)\cos\left(k_{\mathrm{si}}\left(g - \frac{L}{2}\right)\right) - 2\sqrt{\frac{E_{\mathrm{diel}}\rho_{\mathrm{diel}}}{E_{\mathrm{si}}\rho_{\mathrm{si}}}}\sin\left(k_{\mathrm{diel}}\frac{g}{2}\right)\sin\left(k_{\mathrm{si}}\left(d - \frac{g}{2}\right)\right) \times \cos\left(k_{\mathrm{si}}\left(\frac{g}{2} - \frac{L}{2} + d\right)\right) \quad (28)$$

$$N_{B2} = \sin\left(k_{\mathrm{diel}}\frac{g}{2}\right)\cos\left(k_{\mathrm{si}}\left(\frac{L}{2} - 2d\right)\right) \quad (29)$$

$$A_3 = 0, \quad B_3 = -\frac{2\varepsilon_0\varepsilon_r V_{\mathrm{DC}}\sin\left(k_{\mathrm{diel}}\frac{g}{2}\right)}{g^2}\frac{1}{E_{\mathrm{si}}k_{\mathrm{si}}}\frac{N_3}{D}, \quad \text{where} \quad (30)$$

$$N_3 = \sqrt{\frac{E_{\mathrm{diel}}\rho_{\mathrm{diel}}}{E_{\mathrm{si}}\rho_{\mathrm{si}}}}\sin\left(k_{\mathrm{diel}}\frac{g}{2}\right)\sin\left(k_{\mathrm{si}}\left(d - \frac{g}{2}\right)\right) - \cos\left(k_{\mathrm{diel}}\frac{g}{2}\right)\cos\left(k_{\mathrm{si}}\left(d - \frac{g}{2}\right)\right) \quad (31)$$

$$D = \sin(k_{\mathrm{diel}}g) \times\left[\frac{E_{\mathrm{diel}}\rho_{\mathrm{diel}}}{E_{\mathrm{si}}\rho_{\mathrm{si}}}\cos\left(k_{\mathrm{si}}\left(\frac{g}{2} - \frac{L}{2} + d\right)\right)\sin\left(k_{\mathrm{si}}\left(d - \frac{g}{2}\right)\right) - \sin\left(k_{\mathrm{si}}\left(\frac{g}{2} - \frac{L}{2} + d\right)\right)\cos\left(k_{\mathrm{si}}\left(d - \frac{g}{2}\right)\right)\right] - \sqrt{\frac{E_{\mathrm{diel}}\rho_{\mathrm{diel}}}{E_{\mathrm{si}}\rho_{\mathrm{si}}}}\cos(k_{\mathrm{diel}}g)\cos\left(k_{\mathrm{si}}\left(\frac{L}{2} - g\right)\right) \quad (32)$$

In the limit that the dielectric layer and the resonator body material are acoustically matched, $k_{\mathrm{diel}} = k_{\mathrm{si}} = n\pi/L$, $E_{\mathrm{diel}} = E_{\mathrm{si}}$, and $\rho_{\mathrm{diel}} = \rho_{\mathrm{si}}$. The reader can verify that in this acoustically matched limit, the mode shape converges to a perfectly sinusoidal mode shape as predicted by [3], thus verifying that this theory converges to known behavior.

III. Numerical Simulation Results

As mentioned in Section II, finding the motional impedance requires incorporating loss into the system, i.e., including nonzero b_{diel} and b_{si} terms to model the mechanical loss in each region. Previously, we had taken $b_{\mathrm{diel}} = b_{\mathrm{si}} = 0$, which allowed us to choose sine and cosine solutions with purely real wavenumbers k in each region. With nonzero values for these loss coefficients, (7)–(9) indicate that the effective energy storage modulus (simply the Young's modulus for the lossless case) becomes complex. In this case, the same general solution may be used, except k is now a complex wavenumber given by

$$k_{\mathrm{si}} = \beta_{\mathrm{si}} + j\alpha_{\mathrm{si}}, \quad k_{\mathrm{diel}} = \beta_{\mathrm{diel}} + j\alpha_{\mathrm{diel}} \quad (33)$$

$$\beta_{\mathrm{si}} = \frac{\omega}{c_{\mathrm{si}}}, \quad \beta_{\mathrm{diel}} = \frac{\omega}{c_{\mathrm{diel}}}, \quad \alpha_{\mathrm{si}} = \frac{\omega^2 b_{\mathrm{si}}}{2c_{\mathrm{si}}E_{\mathrm{si}}}, \quad \alpha_{\mathrm{diel}} = \frac{\omega^2 b_{\mathrm{diel}}}{2c_{\mathrm{diel}}E_{\mathrm{diel}}}. \quad (34)$$

Here, β now signifies the wave propagation constant and α is a quantity that characterizes the loss per wavelength within the medium. For the following analysis, we will assume for simplicity that $b_{\mathrm{diel}} = b_{\mathrm{si}}$. Qualitatively, this means that for each acoustic wavelength traveled, a longitudinal plane wave traveling through the dielectric material will be attenuated by the same amount as a longi-

tudinal plane wave traveling through silicon. Note that there are a variety of contributions to this loss parameter including viscous air damping, anchor loss, and internal acoustic losses attributable to Akheiser effect and thermoelastic damping, both of which are highly dependent on the crystalline structure of the material. For these reasons, generally $b_{\rm si} \neq b_{\rm diel}$. However, at low frequencies where the acoustic wavelength in the dielectric $\lambda_{\rm diel} \gg g$, we can assume that the difference in energy loss for acoustic waves traveling through the dielectric layer and the surrounding silicon is negligible. As a final note, notice that in the acoustically matched limit, $\beta_{\rm si} = \beta_{\rm diel} = \beta$ and $\alpha_{\rm si} = \alpha_{\rm diel} = \beta/2Q$, where Q is the quality factor of the resonance.

If we assume that the system is low loss (i.e., $E \gg \omega b$), taking the series expansion of D shows that at the resonant frequencies of the system, all real terms in (32) cancel out, D becomes purely imaginary and the magnitude exhibits a local nonzero minimum. This magnitude determines the finite values of the coefficients in (22)–(24). Because of the complex nature of the equations, finding an analytical expression for the magnitude is difficult. Therefore, numerical simulations in MATLAB (The MathWorks, Natick, MA) were used to gain insight into the results of the preceding analysis. For the numerical simulations, we introduce two parameters that characterize the acoustic mismatch between the two materials: r_E and r_ρ, defined as

$$r_E = \sqrt{\frac{E_{\rm diel}}{E_{\rm si}}}, \quad r_\rho = \sqrt{\frac{\rho_{\rm diel}}{\rho_{\rm si}}}\ . \tag{35}$$

The dependence of the motional impedance and resonant frequency on these parameters are found using simulations on a resonator with $L = 12$ μm, corresponding to a 3rd harmonic frequency of 1.067 GHz and an acoustic wavelength of 8 μm in a uniform silicon bar resonator.

First, we sweep the resonant frequency as a function of the dielectric position d and parameterize by both r_E and r_ρ, as shown in Fig. 2. As a verification of our theory, we also use the finite element analysis software COMSOL (Comsol Inc., Burlington, MA) to extract the resonant frequencies of resonators with the same dimensions as described previously. This is done by repeatedly performing a modal analysis (which solves the coupled eigenvalue problem for each finite element of the specified geometry) on the resonator geometry while changing the dielectric position and the parameters r_E and r_ρ. The results of these COMSOL simulations are also included in Fig. 2 and show good agreement with the presented theory. We see from both these plots that the dependence on d is roughly sinusoidal with a wavelength equal to half that of the resonant wavelength in the resonator body. The average value and amplitude of the sinusoid is dependent upon r_E, r_ρ, and g. For $r_E > 1$ or $r_\rho < 1$, the resonant frequency increases with respect to the acoustically matched case ($r_E = r_\rho = 1$). This is expected because the resonator is effectively becoming stiffer or lighter. The opposite is true for $r_E < 1$ or $r_\rho > 1$. Also, as g increases, a larger portion of the resonator is affected by the acoustic mismatch, which explains the increase in frequency deviation with g.

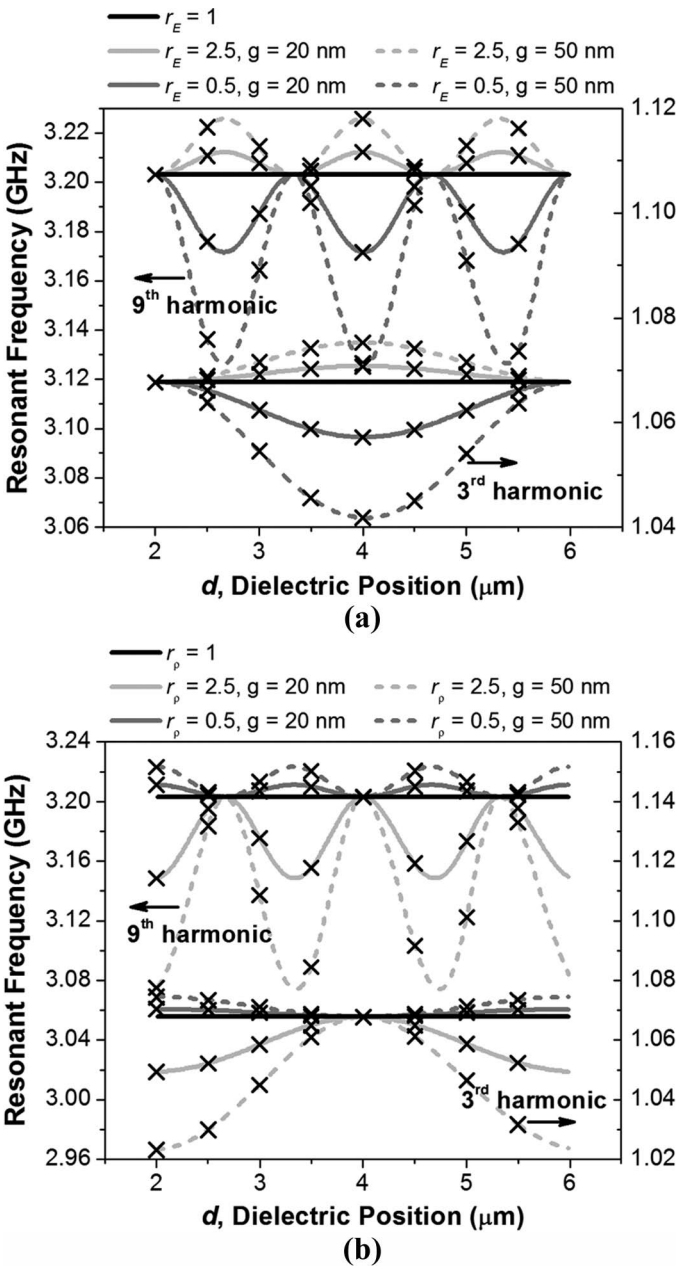

Fig. 2. (a) f_o vs. d with $r_\rho = 1$ and different values of r_E and g for 3rd and 9th harmonic. COMSOL simulation results are overlaid as Xs. (b) f_o vs. d with $r_E = 1$ and different values of r_ρ and g for 3rd and 9th harmonic. COMSOL simulation results are overlaid as Xs.

Close inspection of Figs. 2(a) and 2(b) shows that at displacement nodes, the frequency varies minimally with r_ρ and maximally with r_E. The opposite is also true at displacement maxima. This intuitively suggests that the dielectric film acts as a mass-spring system that couples the inner body and the electrode of the resonator.

A mechanical resonator can be modeled as a distributed network of infinitesimal masses and springs, just like a transmission line is modeled as a network of infinitesimal inductances and capacitances. Because we are assuming that $g \ll \lambda_{\rm diel}$, we can model this whole system as two

transmission lines representing the inner body and the electrode coupled by a mass-spring element, which represents the dielectric film.

This observation helps make sense of the numerical simulation results. At displacement nodes, the coupling mass does not contribute much because it does not move, whereas the coupling spring contribution is large because it is stretched maximally (i.e., maximum strain). On the other hand, at displacement maxima, the strain is minimal so the coupling spring contribution is small whereas the coupling mass contributes greatly because it moves maximally. Note that this is only valid when the thickness of the dielectric film g is small compared with the acoustic wavelength of the dielectric film.

Next, the motional impedance as a function of d and parameterized by both r_E and r_ρ is plotted in Fig. 3. The motional impedance is defined as $R_x = v_{\text{in}}/i_{\text{out}}$ where v_{in} is the input ac voltage that actuates mechanical stress in the device and i_{out} is the output displacement current due to the modulation of the capacitor dielectric thickness. Small values of R_X indicate efficient transduction. Fig. 3 shows a roughly $1/\sin^2(kd)$ dependence of motional impedance on d, much like what is described in [3]. These plots also reveal that the minimum motional impedance is a strong function of r_E but remains roughly constant with r_ρ. In fact, we see that the minimum motional impedance shows a roughly quartic dependence on r_E. Inspection of the magnitudes of the mode shape coefficients via numerical simulation shows that N_i [where $i = 1$, A2, B2, 3 from (25)–(32)] is roughly proportional to r_ρ/r_E, whereas D is roughly proportional to $r_\rho r_E$. Thus, the r_ρ factor cancels out and the resonant amplitude becomes proportional to $r_E{}^{-2}$. Because the output displacement current is proportional to the square of the resonant amplitude as well, the overall proportionality of the motional impedance becomes $r_E{}^4$.

Closer examination of the motional impedance as a function of dielectric position shows that the minimum point of motional impedance depends on r_E and r_ρ. An analytical expression for this shift can be found by solving for the value of d that results in a maximum value of $U_2\ (-g/2) - U_2\ (g/2)$. After applying the simplifying assumptions previously stated (i.e., E_{si}, $E_{\text{diel}} \gg \omega b$, $g \ll \lambda_{\text{diel}}$), a relatively simple expression for the shift in optimal dielectric position d_{opt} can be found. This expression is shown in (36). Fig. 4 shows good agreement between the simulated optimal dielectric position and that predicted by (36). Note that roughness in the simulation results is due to resolution limits in the numerical simulation and improves with better frequency and spatial resolution at the cost of simulation time.

$$\frac{d_{\text{opt,new}}}{d_{\text{opt}}} = \frac{1-\frac{g}{L}}{1-\frac{g}{L}\frac{E_{\text{si}}}{E_{\text{diel}}}}\,\frac{1-\frac{g}{2L}\frac{\rho_{\text{diel}}}{\rho_{\text{si}}}}{1-\frac{g}{2L}} \tag{36}$$

It is worth mentioning at this point the sensitivity of the resonant frequency and motional impedance to process variations that may offset the dielectric film from its optimal position. As seen in Figs. 2 and 3, around minimum displacement points, the derivatives of both resonant frequency and motional impedance with respect to the dielectric placement approach zero. Thus, it seems that resonators properly designed to minimize motional impedance will also exhibit the lowest sensitivity to fabrication tolerances. This is also mentioned in [3]. Ultimately, though, the sensitivity to fabrication tolerances will depend on the acoustic wavelength of the body and electrode material, and in turn the resonant frequency. Mathematically, we see that both $\partial f_o/\partial d$ and $\partial R_X/\partial d \sim k_{\text{si}}{}^2 = 4\pi^2/\lambda_{\text{si}}{}^2$. Intuitively, this is due to the fact that as the frequency increases, the acoustic wavelength decreases, meaning that the same small shift in dielectric

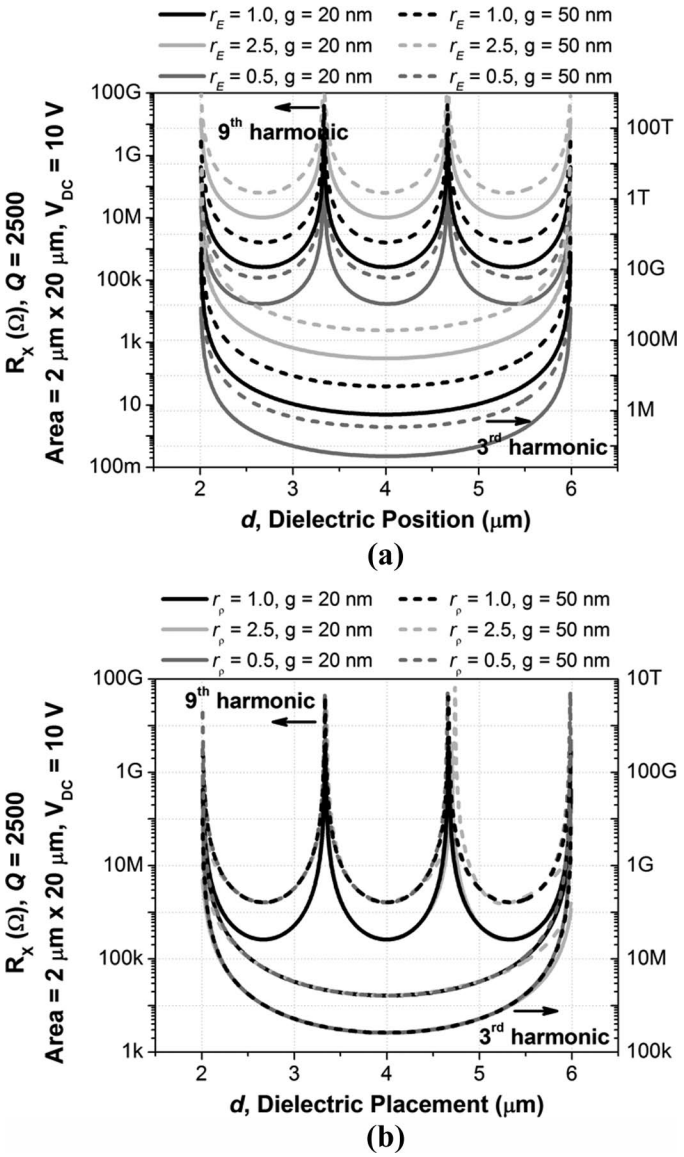

Fig. 3. (a) R_X vs. d with $r_\rho = 1$ and different values of r_E and g for 3rd and 9th harmonic. Assumed parameter values are $Q = 2500$, Area = 20 × 2 μm, and $V_{DC} = 10$ V. (b) R_X vs. d with $r_E = 1$ and different values of r_ρ and g for 3rd and 9th harmonic. Assumed parameter values are $Q = 2500$, Area = 20 × 2 μm, and $V_{DC} = 10$ V.

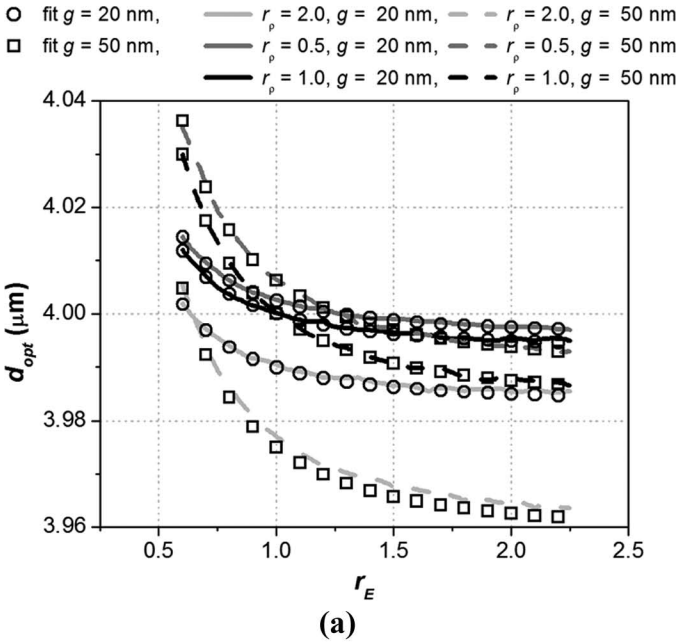

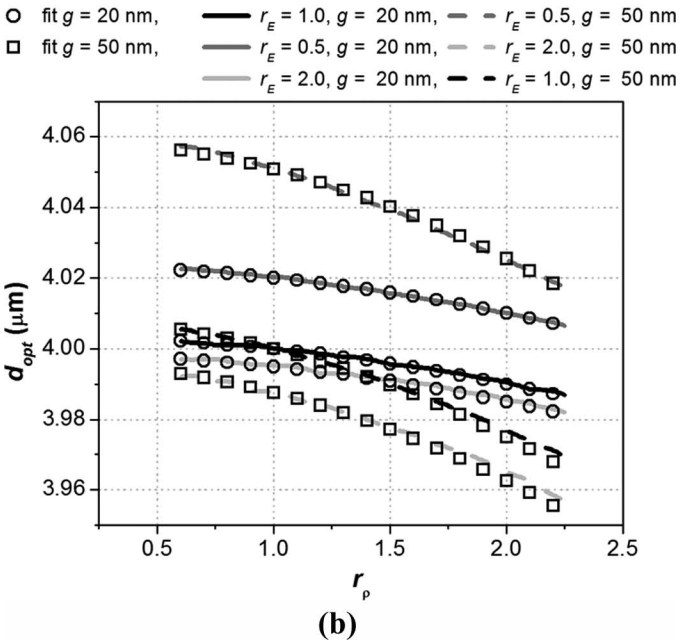

Fig. 4. (a) d_{opt} vs. r_E with $g = 20$ nm for different values of r_ρ at 3rd harmonic. The optimal dielectric position for acoustically matched layers for this device geometry is 4 μm. (b) d_{opt} vs. r_ρ with $g = 20$ nm for different values of r_E at 3rd harmonic. The optimal dielectric position for acoustically matched layers for this device geometry is 4 μm.

placement caused by fabrication tolerances now accounts for a larger portion of the acoustic wavelength. This will lead to a larger sensitivity in both resonant frequency and motional impedance to fabrication tolerances for higher-frequency devices.

Finally, to provide insight into the effects of acoustic mismatch on practical devices, numerical simulations were also conducted on resonators using common dielectric materials such as Si_3N_4 (nitride) and HfO_2 (hafnia). These results are shown below in Fig. 5. Table I lists the minimum motional impedances for different dielectric films

TABLE I. THIRD-HARMONIC MOTIONAL IMPEDANCES FOR VARIOUS DIELECTRICAL MATERIALS ASSUMING $Q = 2500$, AREA $= 20 \times 2$ μM, AND $V_{DC} = 10$ V.

Dielectric	g (nm)	d_{opt} (μm)	$R_{x,\min}$
Acoustically matched	20	4	781 kΩ
$\varepsilon_{\text{diel}} = 7$,	50	4	4.88 MΩ
$E_{\text{diel}} = 170$ GPa,			
$\rho_{\text{diel}} = 2330$ kg/m^3			
Si_3N_4	20	3.997	2.27 MΩ
$\varepsilon_{\text{diel}} = 7$,	50	3.991	14.1 MΩ
$E_{\text{diel}} = 290$ GPa,			
$\rho_{\text{diel}} = 3184$ kg/m^3			
HfO_2	20	3.988	297 kΩ
$\varepsilon_{\text{diel}} = 20$,	50	3.968	1.85 MΩ
$E_{\text{diel}} = 300$ GPa,			
$\rho_{\text{diel}} = 9680$ kg/m^3			
SiO_2	20	4.009	367 kΩ
$\varepsilon_{\text{diel}} = 4$,	50	4.026	2.36 MΩ
$E_{\text{diel}} = 66$ GPa,			
$\rho_{\text{diel}} = 2270$ kg/m^3			

and resonator geometries. Here we see the significance of the quartic dependence of motional impedance on r_E. Although Si_3N_4 has a dielectric constant roughly twice as large as SiO_2, its use results in a much higher motional impedance because it is extremely stiff. Using HfO_2 results in a lower impedance than what is obtained using SiO_2, but not nearly as low as expected if taking into account only the improvement caused by the higher dielectric constant. This indicates that the material stiffness along with the dielectric constant must be considered in choosing the optimal dielectric material.

IV. CORRECTION FACTORS

To find an analytical expression for the shift in resonant frequency, we apply Rayleigh's method and set equal the total kinetic and potential energies within the resonator. Using this method for the acoustically matched condition gives us the typical resonant frequency $f_o = nc_{\text{si}}/2L$ for a longitudinal mode bar resonator. To simplify the math, we assume $g \ll \lambda_{\text{diel}}$, L, which enables us to find a correction to the resonant frequency expressed as

$$\frac{f_{o,\text{new}}}{f_o} = \frac{1 - \frac{2g}{L}\frac{E_{\text{si}}}{E_{\text{diel}}}\cos^2\left(\frac{n\pi d}{L}\right)}{1 - \frac{2g}{L}\cos^2\left(\frac{n\pi d}{L}\right)} \frac{1 - \frac{2g}{L}\sin^2\left(\frac{n\pi d}{L}\right)}{1 - \frac{2g}{L}\frac{\rho_{\text{diel}}}{\rho_{\text{si}}}\sin^2\left(\frac{n\pi d}{L}\right)} \approx \frac{1 - \frac{2g}{L}\frac{E_{\text{si}}}{E_{\text{diel}}}}{1 - \frac{2g}{L}}. \quad (37)$$

For optimal resonator design, the dielectric placement is at a displacement node, meaning that the second factor in (37) becomes almost unity. Thus, we see that for an optimally designed resonator, the density mismatch contributes negligibly to the resonant frequency shift. On the other hand, the mismatch in the Young's moduli signifi-

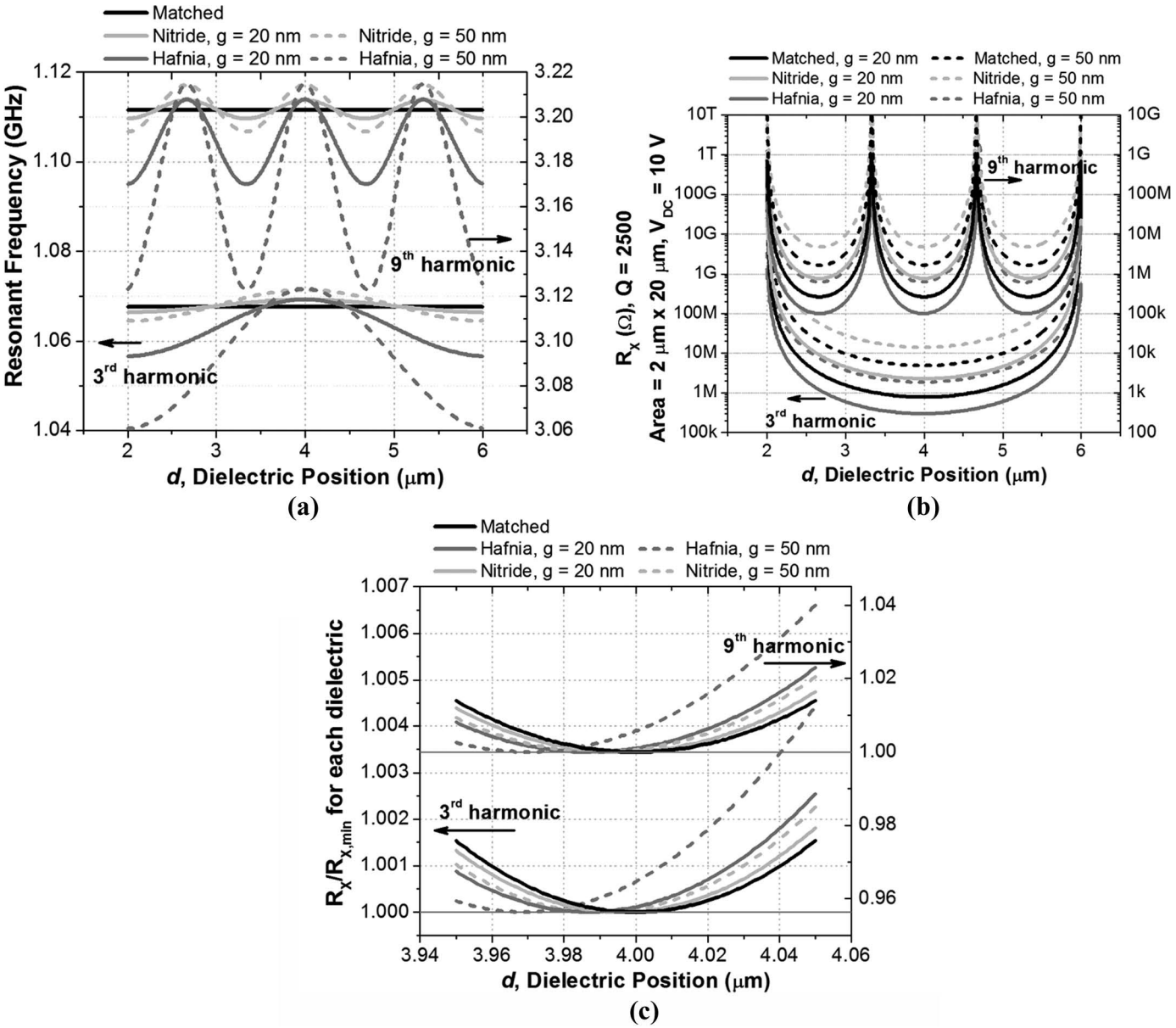

Fig. 5. (a) f_o vs. d for different values of g and dielectric materials at 3rd and 9th harmonic. (b) R_X vs. d for different values of g and dielectric materials at 3rd and 9th harmonic. Assumed parameter values are $Q = 2500$, Area $= 20 \times 2$ μm, and $\mathrm{V_{DC}} = 10$ V. (c) Close-up view of normalized R_X for different dielectric materials.

cantly affects the correction factor in (37) for an optimally designed resonator. This matches well with what is observed from numerical simulations. Similarly, a correction to the motional impedance can be given by

$$R_{x,\mathrm{new}} = \left(\frac{E_{\mathrm{diel}}}{E_{\mathrm{si}}}\right)^2 R_x. \tag{38}$$

Finally, we verify the accuracy of these correction factors by plotting the resonant frequency and motional impedance as a function of r_E for various values of dielectric thickness g in Fig. 6. The dielectric is optimally placed for all plotted results. The results are not plotted with respect to r_ρ because this quantity contributes negligibly for optimally placed dielectrics. Overlaid on the plots are the estimated values for each case using the correction factors in (37) and (38). Figs. 6(c) and 6(d) plot the error in correction factor for both the resonant frequency and motional impedance. We see a maximum frequency error of approximately 1300 ppm and a maximum motional impedance error of approximately 18%. Fig. 6 shows that these maximum errors occur for the lowest plotted values of r_E and decrease steadily until $r_E = 1$, where they approach zero. Beyond that for values of $r_E > 1$, the error seems to approach a steady value. We can see that the error is heavily dependent upon g, which can be attributed to the assumptions used to simplify (37) and (38), specifically that $g \ll \lambda_{\mathrm{diel}}$. Note that these errors are between the 1-D MATLAB model including acoustic mismatch and the correction factors presented in (37) and (38). Neither

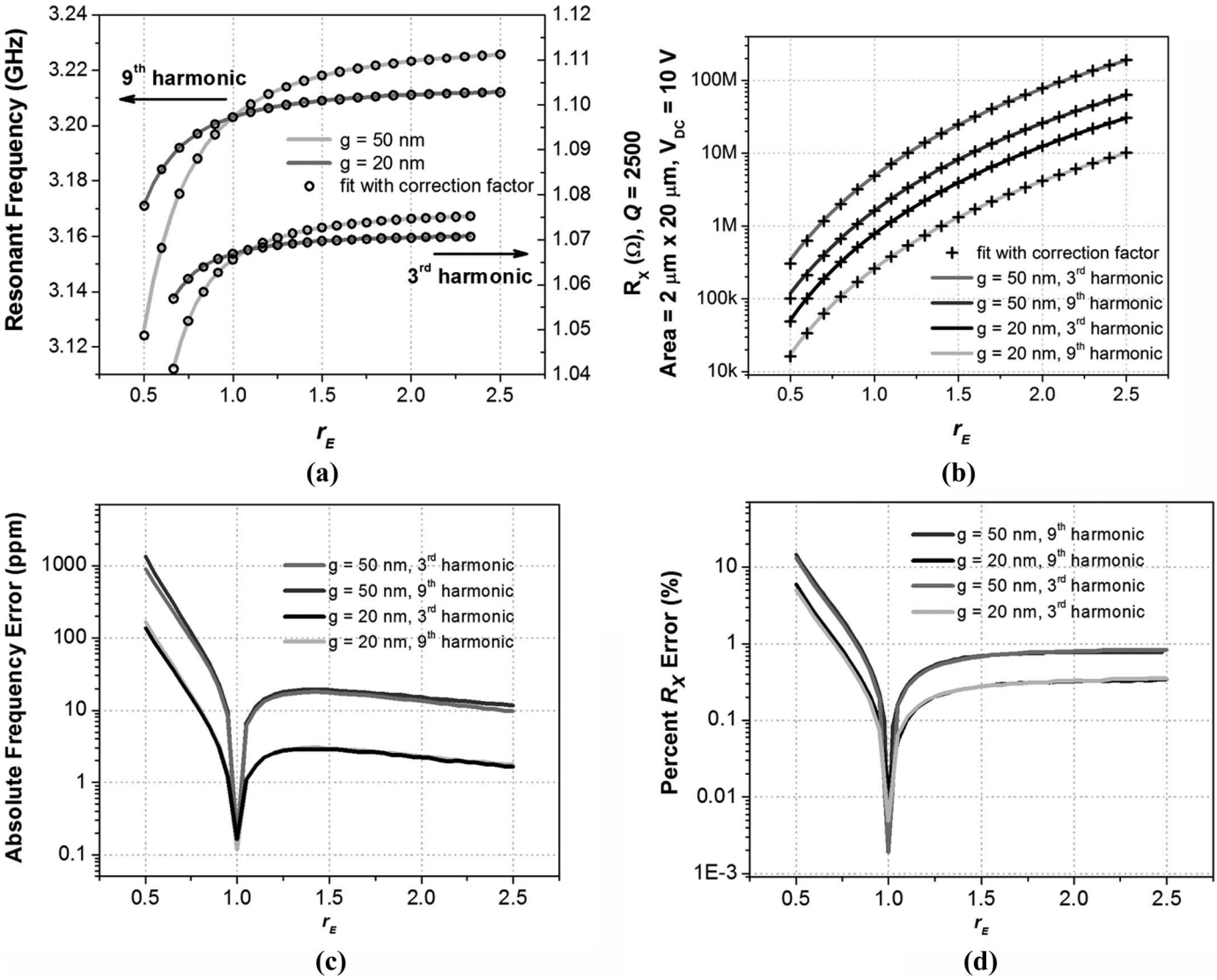

Fig. 6. (a) f_o vs. r_E for different values of g at 3rd and 9th harmonic. (b) R_X vs. r_E for different values of g at 3rd and 9th harmonic. Assumed parameter values are $Q = 2500$, Area $= 20 \times 2$ μm, and $V_{DC} = 10$ V. (c) Percent frequency error between simulated resonant frequency and that estimated by (37). (d) Percent R_X error between simulated motional impedance and that estimated by (38).

of these include the various other effects that could result in larger discrepancies between experimental values and those predicted by the above correction factors, e.g., mode shape distortion caused by the tethers, 2-D effects which cause non-uniform motion of the dielectric boundaries, etc. Finally, one should note that most CMOS-compatible materials that would be good candidates for use in the dielectric layer fall between $0.6 < r_E < 2$. Examples of such materials are SiO_2 and HfO_2, which have values of $r_E = 0.63$ and 1.33, respectively. Fig. 6 shows that the error in resonant frequency within this range is <400 ppm and that the error in motional impedance is <5%, indicating that these simple correction factors are adequate estimates of performance for a wide variety of materials as long as $g \ll \lambda_{\text{diel}}$.

As a final note, the frequency range of applicability of these correction factors should be discussed. Because the derivation of these factors is dependent upon the assumption that $g \ll \lambda_{\text{diel}}$, it would be helpful to explore reasonable dielectric thicknesses to determine the frequency limits to which they may apply. Although efficient transduction pushes the dielectric thickness toward smaller values, realistically, there is a limit dictated by device reliability and manufacturability. Specifically, as the dielectric thickness is scaled to smaller values, the risks associated with dielectric breakdown increase, severely limiting the device reliability and lifetime. In addition, thinner dielectric layers result in larger tunneling current, which acts to reduce the voltage drop across the transducer and thus degrade performance. Taking these limitations into account, realistic dielectric thicknesses may be on the order of 10 nm. Using silicon nitride ($c_{\text{diel}} = 9543$ m/s) as an example and assuming the correction factors are valid for values of $\lambda_{\text{diel}}/g > 10$, this results in a valid frequency range of roughly 95 GHz. Although this value is dependent upon the dielectric material used and the required accuracy in

estimating the frequency and motional impedance for the particular application at hand, we see that these correction factors are typically valid for operation of internal dielectrically transduced micromechanical resonators up to tens of gigahertz. Here, an important distinction must be made between the validity of the analysis presented in this paper and the validity of the correction factors presented. Although the initial analysis remains valid for low-loss silicon resonators for all frequencies, the presented correction factors for the optimal dielectric position, resonant frequency, and motional impedance are only valid when $g \ll \lambda_{\text{diel}}$, or up to tens of gigahertz, as discussed. The initial analysis and corresponding numerical analysis using MATLAB is still valid to find the resonant frequency and motional impedance even when the condition $g \ll \lambda_{\text{diel}}$ is not satisfied, albeit only numerically.

V. Conclusions

In summary, this paper presents a supplement to the theory presented in [3] for internal dielectrically transduced micromechanical resonators that includes the effects of acoustic mismatch on resonator performance. This paper also provides correction factors to provide a simple yet accurate set of design equations. The intuition provided in this paper indicates that for optimally designed resonators, to first order, only the mismatch in the Young's moduli affects the properties of the resonator. Although the exact theory in this paper is specific to a bar resonator, this insight can be extended to any similar composite bulk-mode resonator like those shown in [5] and [6]. Also, we have highlighted the importance of the Young's moduli mismatch in selecting dielectric materials for optimal transduction efficiency. These insights should help designers optimize designs for internal dielectrically transduced micromechanical resonators for use in larger systems.

References

[1] S.-S. Li, Y.-W. Lin, Z. Ren, and C. T.-C. Nguyen, "An MSI micromechanical differential disk-array filter," in *Proc. 14th Int. Conf. Solid–State Sensors, Actuators, and Microsystems*, Jun. 10–14, 2007, pp. 307–311.

[2] G. Piazza, P. J. Stephanou, and A. P. Pisano, "Piezoelectric aluminum nitride vibrating contour-mode MEMS resonators," *J. Microelectromech. Syst.*, vol. 15, no. 6, pp. 1406–1418, Dec. 2006.

[3] D. Weinstein and S. A. Bhave, "Internal dielectric transduction: Optimal position and frequency scaling," *IEEE Trans. Ultrason. Ferroelectr. Freq. Control*, vol. 54, no. 12, pp. 2696–2698, Dec. 2007.

[4] D. Weinstein, S. A. Bhave, S. Morita, S. Mitarai, and K. Ikeda, "Frequency scaling and transducer efficiency in internal dielectrically transduced silicon bar resonators," in *Proc. 15th Int. Conf. Solid–State Sensors, Actuators, and Microsystems*, Jun. 21–25, 2009, pp. 708–711.

[5] Y.-W. Lin, S.-S. Li, Y. Xie, Z. Ren, and C. T.-C. Nguyen, "Vibrating micromechanical resonators with solid dielectric capacitive transducer gaps," in *Proc. 2005 IEEE Int. Frequency Control Symp.*, Aug. 29–31, 2005, pp. 128–134.

[6] M. Ziaei-Moayyed, D. Elata, J. Hsieh, J.-W. P. Chen, E. P. Quévy, and R. T. Howe, "Fully differential internal electrostatic transduction of a Lamé-mode resonator," in *Proc. 22nd IEEE Int. Conf. Micro Electro Mechanical Systems*, Jan. 25–29, 2009, pp. 931–934.

[7] V. Kaajakari, A. T. Alastalo, and T. Mattila, "Electrostatic transducers for micromechanical resonators: free space and solid dielectric," *IEEE Trans. Ultrason. Ferroelectr. Freq. Control*, vol. 53, no. 12, pp. 2484–2489, Dec. 2006.

[8] K. F. Graff, *Wave Motion in Elastic Solids*. New York: Dover, 1975.

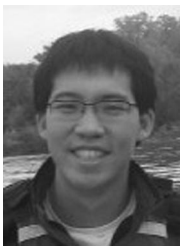

Eugene Hwang (S'06) received the B.S. degree in electrical engineering and computer sciences at the University of California, Berkeley in 2006 and is currently pursuing a Ph.D. in electrical and computer engineering at Cornell University. His research interests include low-power RF and analog circuit design, micromechanical systems for RF applications, MEMS-CMOS integration, and nonlinear dynamics in microscale mechanical devices.

Sunil A. Bhave (S'99–M'04) received the B.S. and Ph.D. degrees in electrical engineering and computer sciences from the University of California, Berkeley, in 1998 and 2004, respectively. In October 2004, he joined the faculty of Cornell University, Ithaca, NY, where he is currently an Assistant Professor in the School of Electrical and Computer Engineering. His research interests focus on MEMS resonators for radio front ends, merged CMOS-NEMS for low-power computation, inertial and acoustic sensors, and hybrid photonic NEMS and magnetic NEMS for low-phase-noise microwave oscillators. Prof. Bhave was the recipient of the NSF Early CAREER Development Award in 2007 and the DARPA Young Faculty Award in 2008. Along with his students, he has been awarded the Roger A. Hakan Best Paper Award at IEDM 2007 and is the winner of the Student Paper Competition at the 2009 IEEE International Ultrasonics Symposium.